Femtosecond pulse shaping using plasmonic snowflake nanoantennas

Rüştü Umut Tok and Kürşat Şendur*
Sabancı University, Orhanlı-Tuzla, 34956, Istanbul, Turkey
(Received 25 June 2011; published 22 September 2011)

We have theoretically demonstrated femtosecond pulse manipulation at the nanoscale using the plasmonic snowflake antenna's ability to localize light over a broad spectrum. To analyze the interaction of the incident femtosecond pulse with the plasmonic nanoantenna, we first decompose the diffraction limited incident femtosecond pulse into its spectral components. The interaction of each spectral component with the nanoantenna is analyzed using finite element technique. The time domain response of the plasmonic antenna is obtained using inverse Fourier transformation. It is shown that the rich spectral characteristics of the plasmonic snowflake nanoantenna allow manipulation of the femtosecond pulses over a wide spectrum. Light localization around the gap region of the nanoantenna is shown for femtosecond pulses. As the alignment of incident light polarization is varied, different antenna elements oscillate, which in turn creates a different spectrum and a distinct femtosecond response.

DOI: 10.1103/PhysRevA.84.033847 PACS number(s): 42.65.Re, 78.20.Bh, 84.40.Ba

I. INTRODUCTION

Fourier transformation-based pulse shaping has been used for the manipulation of femtosecond pulses [1]. Phase and amplitude shaping of the femtosecond pulses allow control and manipulation of quantum-mechanical systems [2–6]. Other potential applications include wideband data transmission in optical communication, biomedical optical imaging, ultrafast computing, high-power laser amplifiers, and laser-electron beam interactions. A large majority of the studies in the literature focus on programmable pulse shaping methods using Fourier techniques, as summarized in a review article by Weiner [1]. Polarization-based pulse shaping methods in the literature utilize optical lenses, which are limited by the diffraction limit of bulk optical elements.

Nanostructures can be utilized to overcome the spatial limitation when used with femtosecond pulses [7,8]. Stockman *et al.* utilized phased modulation of an illumination pulse to achieve coherent control of a spatial distribution since the surface plasmon excitations of nanostructures are correlated with their phase [7,8]. In a more recent study, Aeschlimann *et al.* [9] experimentally demonstrated the feasibility of optical manipulation at the nanoscale through adaptive polarization shaping of the incident beams. In their study, Aeschlimann *et al.* [9] utilized polarization-shaped ultrashort laser pulses, illuminating planar nanostructures to achieve subwavelength control of optical fields. The optical near-field distribution of silver nanostructures was manipulated through adaptive polarization shaping of the femtosecond pulses. Other studies on femtosecond pulse shaping in the literature utilized plasmonic tips and nanostructures [10–15], asymmetric dipole antennas [16], sun-shaped planar nanostructures [17], apertures [18], slit arrays [19], and metamaterials [20]. Related studies on the interaction of metallic nanoparticles with ultrafast pulses include ultrafast active plasmonics [21], attosecond plasmonic microscobe [22], laser-induced nanostructure formation and control of metallic nanoparticle color via ultrafast pulses [23,24], femtosecond surface plasmon pulse propagation on metal-dielectric waveguides [25], dynamics of surface plasmon polaritons in plasmonic crystals [26], and nanoscale ultrafast spectroscopy [27].

As the desired pulse length gets shorter, its spectral distribution gets broader. To achieve and better manipulate ultrashort pulses at the nanoscale, near-field radiators that can localize light over a broad spectrum are essential. In this work, we achieve polarization-based femtosecond pulse shaping using plasmonic snowflake nanoantennas. Nanoantennas have been previously utilized for light localization at the nanoscale for various applications as discussed in recent review articles [28,29]. As recently demonstrated, light localization over a wide spectral regime has been achieved using plasmonic snowflake nanoantennas [30]. The ability to manipulate the spectral distribution of optical spots at the nanoscale has important implications for tailoring ultrashort pulses. In this work, we demonstrate that the plasmonic snowflake antennas [30] can provide control and manipulation of the ultrashort pulses at the nanoscale using their ability to localize light over a broad spectrum.

II. METHODOLOGY

An eight-particle plasmonic snowflake antenna is illuminated with a femtosecond pulse as shown in Fig. 1. The incident beam onto the nanoantenna is diffraction limited. In this study, the incident femtosecond pulse is represented as

$$\vec{E}^i(\vec{r},t) = \mathrm{Re}\left\{ \vec{P}(\vec{r}) \exp[i\vec{k}\vec{r} - i\omega(t - T/2)] \times \left[1 - \frac{3}{2}\left(\frac{(t-T)}{T} \right)^2 \right] \right\}, \quad (1)$$

where T is the duration of the envelope of the femtosecond pulse, the operator $\mathrm{Re}(\cdot)$ represents the real part, ω is the central frequency, $\vec{k}$ is the propagation direction of the incident optical pulse, and $\vec{P}(\vec{r})$ represents the polarization-dependent aspect of the femtosecond pulse. The incident beam defined by Eq. (1) is similar to those in Refs. [7,8] with the exception that the chirping coefficient is set to zero; i.e., the effects of positive

*sendur@sabanciuniv.edu

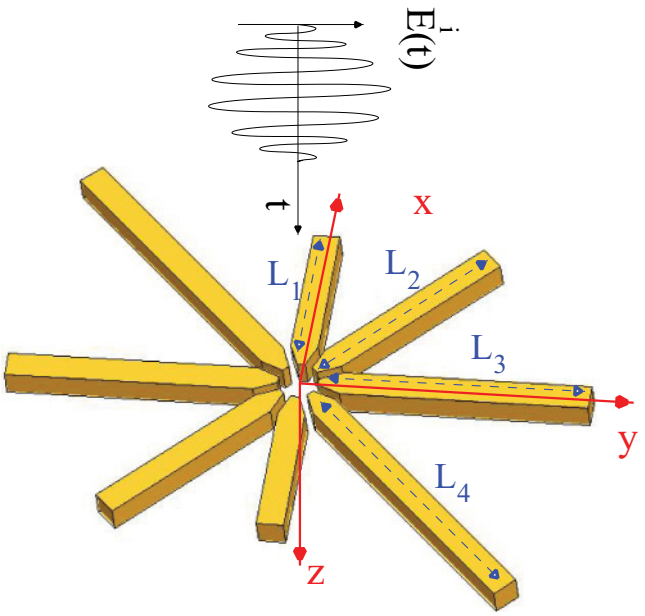

FIG. 1. (Color online) A schematic representation of the eight-particle plasmonic snowflake antenna illuminated with a femtosecond pulse.

and negative chirping are not taken into account. In this study, the pulse duration is $T = 20$ femtoseconds, $\omega = 1.2$ eV, and the propagation direction of the incident pulse is $\hat{z}$, which is normal to the antenna, as shown in Fig. 1. The amplitude of the incident beam is plotted in Fig. 2(a) with these parameters. In this study, the polarization vector $\vec{P}(\vec{r})$ in Eq. (1) is selected as

$$\vec{P}(\vec{r}) = \frac{1}{\sqrt{\xi^2+1}}\hat{x} + \frac{\xi}{\sqrt{\xi^2+1}}\hat{y}, \tag{2}$$

which yields various alignments of the incident electric field vector.

To analyze the interaction of the incident femtosecond pulse in Eq. (1) and the plasmonic nanoantenna, we first decomposed the diffraction limited incident femtosecond pulse into its spectral components

$$\vec{E}^i(\vec{r},\omega) = \int \vec{E}^i(\vec{r},t)\exp(-iwt)dt. \tag{3}$$

For the incident femtosecond pulse $\vec{E}^i(\vec{r},t)$ shown in Fig. 2(a), the corresponding spectral amplitude $\vec{E}^i(\vec{r},\omega)$ is plotted in Fig. 2(b). To analyze the interaction of each frequency component $\vec{E}^i(\vec{r},w)$ with the nanoantenna, a 3D frequency-domain finite element method is utilized [31,32]. The incident field $\vec{E}^i(\vec{r},w)$ represents the optical beam in the absence of the nanoantenna. Once the incident field interacts with the nanoantenna, scattered fields $\vec{E}^s(\vec{r},w)$ are generated. The total electric field $\vec{E}^t(\vec{r},w)$ is composed of the summation of two components, $\vec{E}^i(\vec{r},w)$ and $\vec{E}^s(\vec{r},w)$. To obtain the scattered field $\vec{E}^s(\vec{r})$, we used a 3D finite element method (FEM)-based full-wave solution of Maxwell's equations [31,32]. The scattering geometries in the computational domain are discretized into tetrahedral elements. The medium surrounding the antenna is selected as a vacuum. On the tetrahedral elements, edge basis functions and second-order interpolation

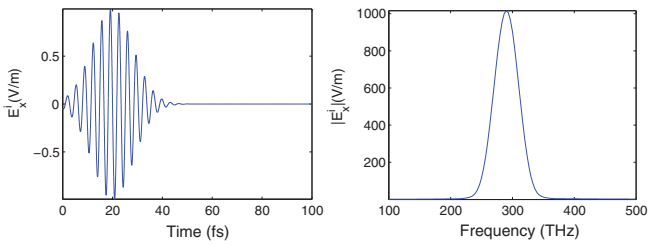

FIG. 2. (Color online) (a) The amplitude of the incident beam as a function of time $|\vec{E}^i(\vec{r},t)|$, and (b) the corresponding spectral amplitude $|\vec{E}^i(\vec{r},\omega)|$.

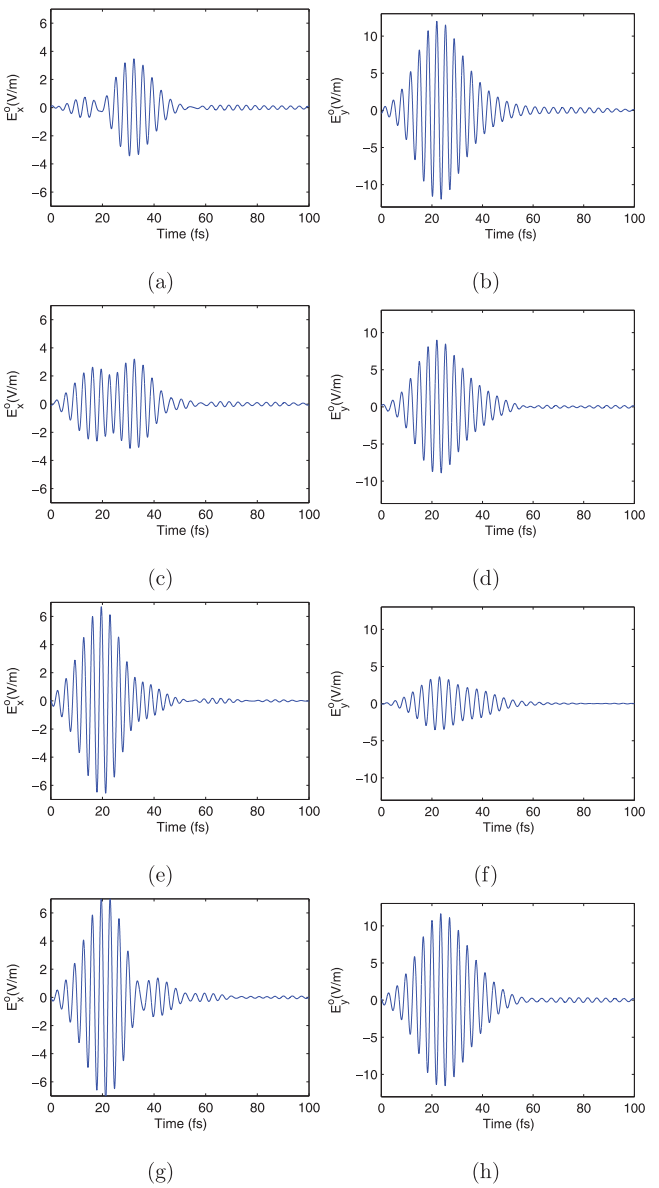

FIG. 3. (Color online) Temporal evolution of the gap field for various polarizations of the incident beam: (a) $\vec{E}_x^o(\vec{r},t)$ for $\xi = -2$, (b) $\vec{E}_y^o(\vec{r},t)$ for $\xi = -2$, (c) $\vec{E}_x^o(\vec{r},t)$ for $\xi = -1$, (d) $\vec{E}_y^o(\vec{r},t)$ for $\xi = -1$, (e) $\vec{E}_x^o(\vec{r},t)$ for $\xi = 0$, (f) $\vec{E}_y^o(\vec{r},t)$ for $\xi = 0$, (g) $\vec{E}_x^o(\vec{r},t)$ for $\xi = 1$, (h) $\vec{E}_y^o(\vec{r},t)$ for $\xi = 1$.

functions are used to expand the unknown functions. Adaptive mesh refinement is used to improve the coarse solution regions with high field intensities and large field gradients. Once the scattered field $\vec{E}^s(\vec{r},w)$ is solved, the total field is obtained by adding the incident field $\vec{E}^i(\vec{r},w)$ to the scattered field $\vec{E}^s(\vec{r},w)$. Once the solution for each frequency ω is obtained, the time domain response of the plasmonic antenna is obtained using the inverse Fourier transformation.

III. RESULTS

An ultrafast incident pulse has a broad spectrum, which necessitates that the interacting structure has a wide-range spectral response in order to manipulate the ultrafast pulses effectively. In Fig. 3, we illustrate the femtosecond manipulation of nanoscale optical spots using the polarization of the incident beam and a plasmonic snowflake antenna with a wide spectral response. The temporal evolution of the gap-field at the center of the nanoantenna is shown in Fig. 3 for various incident beam polarizations. The incident beam propagates in the $\hat{z}$ direction, resulting in normal incidence onto the antenna. The antenna dimensions are selected as $L_1 = 120$ nm, $L_2 = 160$ nm, $L_3 = 200$ nm, and $L_4 = 240$ nm. Gold is selected as the nanoantenna material and the frequency-dependent material properties of gold are taken into account by utilizing the experimental data by Palik [33]. Incident polarizations are varied by selecting ξ values as -2, -1, 0, and 1, for which the tip of the incident field $\vec{E}^i(\vec{r},t)$ traces different polarization lines in time. For $\xi = -1$, the polarization vector is aligned with the antenna denoted L_4, whereas for $\xi = 1$ the polarization vector is aligned with the antenna denoted L_2. As illustrated in Fig. 3, the temporal distribution of the gap-field is significantly modified by selecting different ξ values. The manipulation of the gap-field is due to the spectrally rich response of the plasmonic snowflake nanoantenna. Spectral distributions under various polarizations are primarily controlled by the antenna arm that is parallel to the incident polarization vector $\vec{P}(\vec{r})$. The coupling between dipole antenna pairs, i.e., coupling between L_1, L_2, L_3, and L_4, is small. Changing the ξ values leads to the alignment of the incident polarization vector with different antenna elements, which results in spectral variations. These spectral variations cause differences in the temporal response of the ultrashort gap-fields, which are localized at the nanoscale.

In Fig. 4, the spectral response of the nanoantenna under various incident beam polarizations is presented. In Fig. 4, $H(w)$ is defined at the center of the antenna gap as $H(w) = |E^o(w)|^2/|E^i(w)|^2$, which is a unitless quantity. The spectral response of the nanoantennas demonstrates the multiresonant characteristics of the antenna. Various peaks observed in the spectral response correspond to the resonance of different dipole pairs with differing lengths. The corresponding spectral peaks of individual dipole antennas are highlighted at the top of Fig. 4. Due to weak coupling between different dipole pairs, there is a very small shift in the dipole pairs when they are brought around the common gap. Since the length variation between the dipole pairs is relatively small (40 nm),

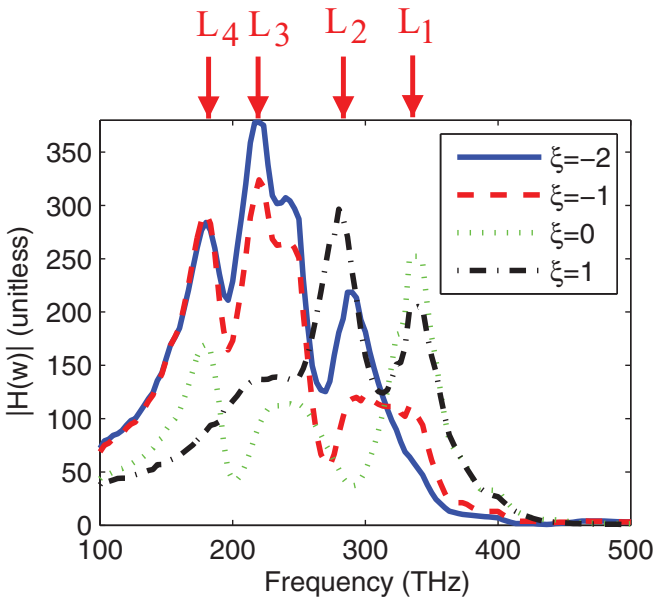

FIG. 4. (Color online) The spectral response of the nanoantenna under various incident beam polarizations.

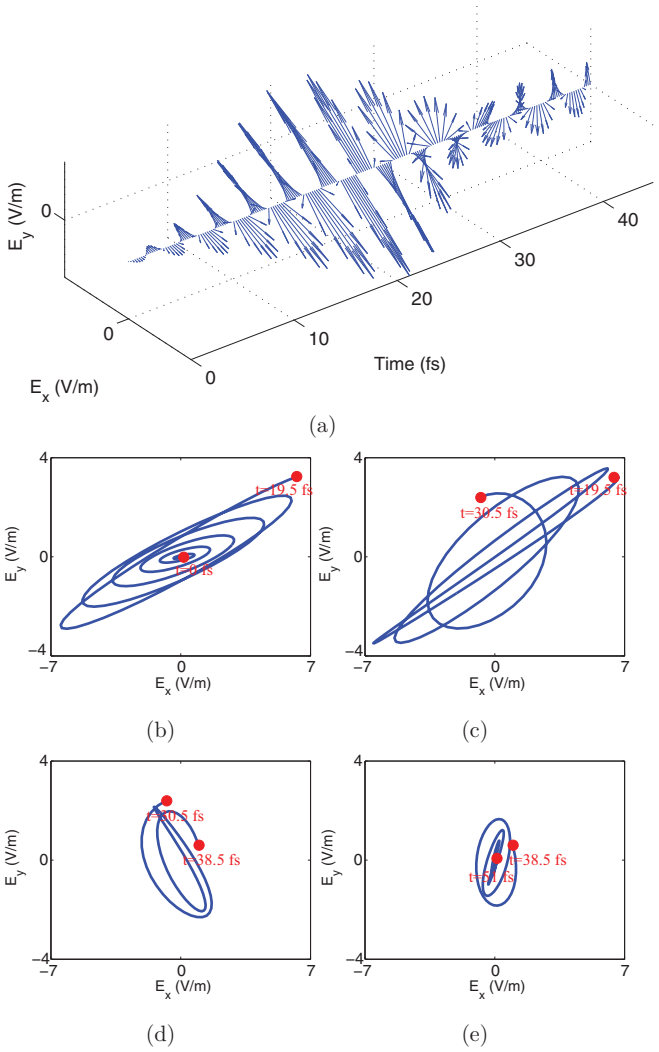

FIG. 5. (Color online) (a) Vectoral plot of the electric field as a function of time for $\xi = 0$. The trace of the tip of the electric field vector in the intervals: (b) t∈ [0, 19.5] fs, (c) t∈ [19.5, 30.5] fs, (d) t∈ [30.5, 38.5] fs, (e) t∈ [38.5, 51] fs.

the resulting spectral peaks are close to each other, resulting in a rich spectral response in the 150–350 THz range. In Fig. 4, various ξ values correspond to different incident polarizations, for which the tip of the electric field vector traces a different line as time progresses. These alignment variations for various ξ values result in different spectral responses. Although the alignment of the incident polarization with various antenna components is a major factor, the antenna spectral response alone does not determine the gap field spectrum and time-dependent gap field. The gap-field spectrum is also determined by scaling the antenna spectral response with the incident beam spectrum in Fig. 2(b). The incident beam spectrum has a central peak around 290 THz with a spectral range between 240 and 340 THz. As a result, the peak corresponding to L_2 has the strongest contribution to the temporal responses in Fig. 3, whereas the spectral peaks corresponding to L_1 and L_3 are weaker and L_4 is the most suppressed.

The temporal shape of the ultrashort gap-fields in Fig. 3 can be further interpreted using Figs. 4 and 2(b) along with fundamental properties of Fourier transformation. The temporal response of the antenna gap-field $E^o(t)$ is most similar to the input excitation when $\xi = 0$. This can be attributed to a property of Fourier transformation, which states that as the spectral response becomes broader and more uniform, the time response gets narrower. For $\xi = 0$, the spectral response of the gap-field $E^o(w)$ is more uniformly distributed compared to the other cases. When the antenna spectral response in Fig. 4 is scaled with the input spectrum in Fig. 2(b), it results in an even more uniform distribution for $\xi = 0$ when compared to the other ξ values. A broad and uniform spectral response causes a narrow time response, which results in the preservation of the output response in a convolution operation. Another important property of Fourier transformation establishes a relationship between the width of the temporal and the associated spectral distributions. As the ultrashort pulses get shorter, the incident beam spectrum becomes broader. This implies that the broad antenna spectrum in Fig. 4 has the capability of manipulating much shorter pulses due to its broad spectrum. The spectral response of the snowflake antenna can be controlled by changing the dimension and the number of particles of the antenna. The spectral peaks corresponding to different antenna pairs can be shifted to higher or lower wavelengths by increasing or decreasing the corresponding antenna length. The spectral response can be broadened by increasing the variation between the antenna lengths. The number of peaks in the spectrum can be increased or decreased by adding or removing the antenna pairs around the common gap.

Figure 5(a) illustrates a vector plot of the electric field as a function of time for $\xi = 0$. The electric field polarization shows different behaviors in various intervals. Figures 5(b)–5(e) show the trace of the tip of the electric field vector in the intervals t$\in$ [0, 19.5] fs, t$\in$ [19.5, 30.5] fs, t$\in$ [30.5, 38.5] fs, and t$\in$ [38.5, 51] fs, respectively. Different polarizations can be identified in various time intervals. In Fig. 5(b), the electric field is elliptically polarized with its major axis aligned in between the x-y axis. In this interval, the polarization does not change and the intensity increases as time progresses. Polarization of the electric field does not change in Fig 5(e), while the intensity decreases as time progresses. In Figs. 5(c) and 5(d), the tip of the electric field vector shows substantial variation as the polarization changes between different elliptical states.

One of the features of the nanosystem in Fig. 1 is its ability to concentrate the ultrafast incident beam to a nanoscale spot beyond the diffraction limit. Spatiotemporal graphs in Figs. 6

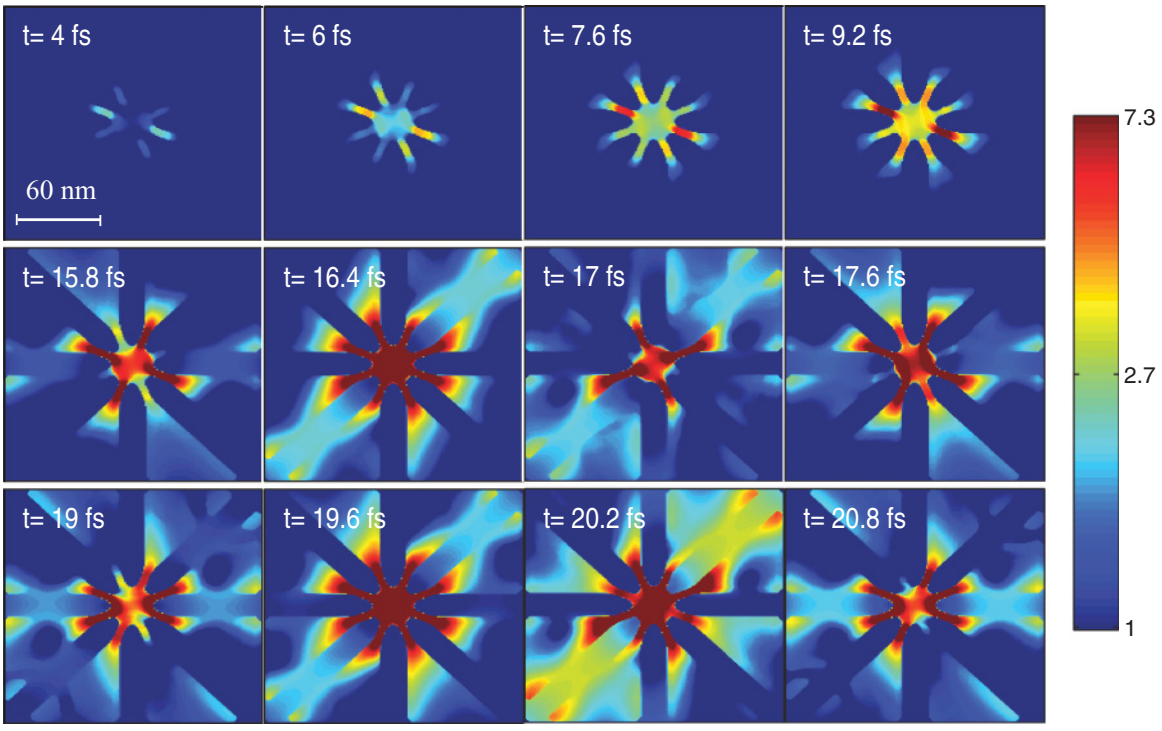

FIG. 6. (Color online) Electric field intensity distribution on the $\hat{x}$-$\hat{y}$ cut plane for $\xi = 1$ at various time instances.

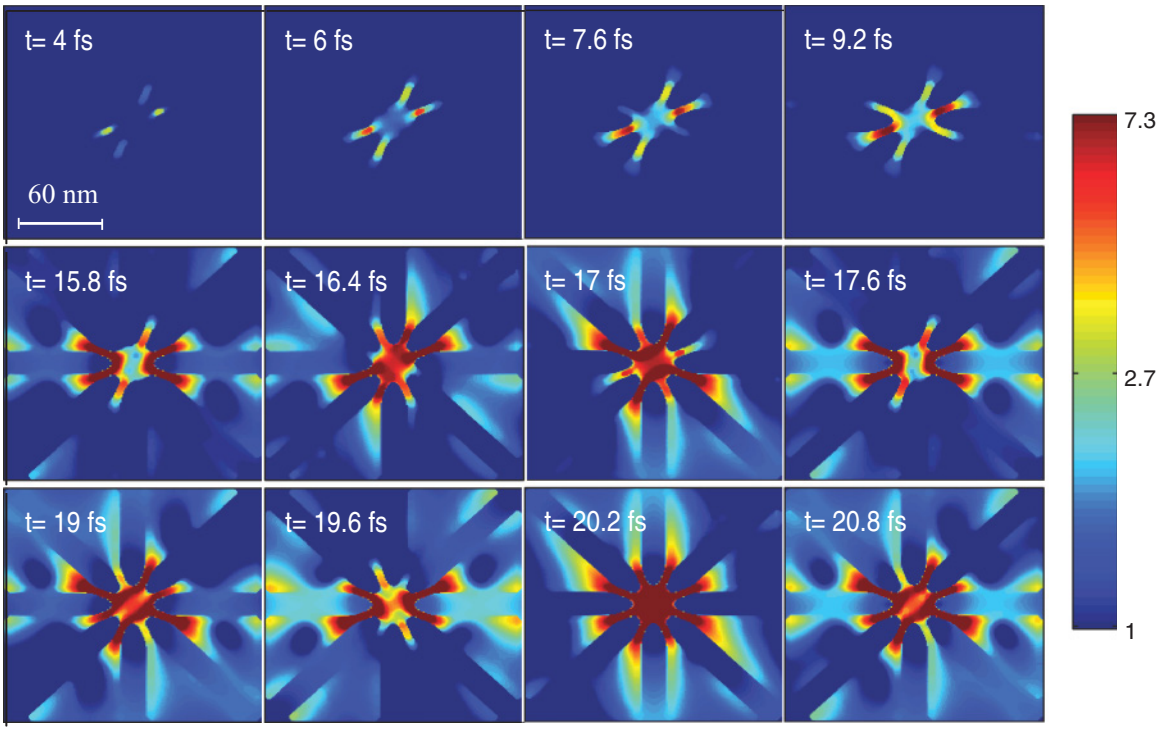

FIG. 7. (Color online) Electric field intensity distribution on the $\hat{x}$-$\hat{y}$ cut plane for $\xi = -1$ at various time instances.

and 7 illustrate the temporal evolution of the optical fields that are confined around the gap region of the nanoantenna on the $\hat{x}$-$\hat{y}$ plane. The colorbars in Figs. 6 and 7 indicate the strength of the electric field compared to that of the incident beam. The electric field distributions in Figs. 6 and 7 are plotted on a logarithmic scale. Figures 6 and 7 correspond to $\xi = 1$ and $\xi = -1$, respectively. For both cases, the optical fields are well localized in the gap region. For $\xi = -1$ and $\xi = 1$, the linearly polarized light excites different arms of the nanoantenna. For $\xi = 1$, the incident beam polarization traces a line that is aligned with the L_2 arm. As a result, plasmonic oscillations associated with the L_2 antenna pair localize the optical energy in the gap region. As shown in Fig. 6, the strongest oscillations are associated with the L_2 arm. The output spectrum is a result of scaling Fig. 4 with Fig. 2(b). The spectral response of the antenna in Fig. 4 has peaks at 290 and 350 THz for $\xi = 1$, which correspond to the L_2 and L_1 arms, respectively. The input spectrum in Fig. 2(b) has a peak at 290 THz, which favors the L_2 peak in Fig. 4. As a result, the strongest resonance in Fig. 6 is observed for the L_2 antenna, with a weaker contribution from the L_1 antenna. The spatiotemporal graphs in Fig. 6 show weak oscillations at $t = 4$ fs. At times $t = 6,7.6$, and 9.2 fs, the temporal oscillations become stronger, primarily due to the contributions from the L_2 and L_1 antennas, as the alignment of the gap field indicates. As time progresses, the antenna gap field gets stronger as shown in Fig. 6. At times $t = 16.4,17,19.6$, and 20.2 fs, the L_2 antenna shows strong resonances, whereas at times $t = 15.8,17.6,19$, and 20.8 fs, the L_1 antenna resonance dominates.

For $\xi = -1$, the linearly polarized radiation traces a line that is aligned with the L_4 arm as time progresses. However, the contributions in Fig. 7 due to the L_4 antenna have a strength similar to L_1 and L_3 due to the scaling of the antenna spectrum with the incident beam spectrum. As a result, the temporal signature of the femtosecond gap field has equal contributions from L_1, L_3, and L_4 antennas.

IV. CONCLUSION

In summary, rich spectral characteristics of the plasmonic snowflake nanoantennas show a strong polarization dependence, which allows the manipulation of the femtosecond pulses over a wide spectrum. Light localization around the gap region of the nanoantenna is obtained for the femtosecond pulses. As the alignment of incident light polarization is varied, different antenna elements resonate, which in turn create a different spectrum and a distinct femtosecond response.

ACKNOWLEDGMENTS

This work is supported by TUBITAK under Project Nos. 108T482 and 109T670 and by European Community Marie Curie International Reintegration Grant No. MIRG-CT-2007-203690. K.S. acknowledges partial support from the Turkish Academy of Sciences.

[1] A. M. Weiner, Rev. Sci. Instrum. **71**, 1929 (2000).
[2] R. S. Judson and H. Rabitz, Phys. Rev. Lett. **68**, 1500 (1992).
[3] A. Assion, T. Baumert, M. Bergt, T. Brixner, B. Kiefer, V. Seyfried, M. Strehle, and G. Gerber, Science **282**, 919 (1998).

[4] D. Meshulach and Y. Silberberg, Nature (London) **396**, 239 (1998).
[5] T. C. Weinacht, J. Ahn, and P. H. Bucksbaum, Nature (London) **397**, 233 (1999).
[6] T. Brixner, N. H. Damrauer, P. Niklaus, and G. Gerber, Nature (London) **414**, 57 (2001).
[7] M. I. Stockman, S. V. Faleev, and D. J. Bergman, Phys. Rev. Lett. **88**, 067402 (2002).
[8] M. I. Stockman, D. J. Bergman, and T. Kobayashi, Phys. Rev. B **69**, 054202 (2004).
[9] M. Aeschlimann, M. Bauer, D. Bayer, T. Brixner, F. J. Garcia de Abajo, W. Pfeiffer, M. Rohmer, C. Spindler, and F. Steeb, Nature (London) **446**, 301 (2007).
[10] T.-W. Lee and S. K. Gray, Phys. Rev. B **71**, 035423 (2005).
[11] T. Brixner, F. J. Garcia de Abajo, J. Schneider, C. Spindler, and W. Pfeiffer, Phys. Rev. B **73**, 125437 (2006).
[12] X. Li and M. I. Stockman, Phys. Rev. B **77**, 195109 (2008).
[13] M. Durach, A. Rusina, M. I. Stockman, and K. A. Nelson, Nano Lett. **7**, 3145 (2007).
[14] P. Tuchscherer, C. Rewitz, D. V. Voronine, F. J. Garcia de Abajo, W. Pfeiffer, and T. Brixner, Opt. Express **17**, 14235 (2009).
[15] S. Berweger, J. M. Atkin, X. G. Xu, R. L. Olmon, and M. B. Raschke, in Conference on Lasers and Electro Optics p. QTuH3 (2011).
[16] J. S. Huang, D. V. Voronine, P. Tuchscherer, T. Brixner, and B. Hecht, Phys. Rev. B **79**, 195441 (2009).
[17] M. Aeschlimann *et al*., Proc. Natl. Acad. Sci. USA **107**, 5329 (2010).
[18] F. I. Baida, Opt. Express **18**, 14812 (2010).
[19] A. Dechant and A. Y. Elezzabi, Appl. Phys. Lett. **84**, 4678 (2004).
[20] T. S. Kao, S. D. Jenkins, J. Ruostekoski, and N. I. Zheludev, Phys. Rev. Lett. **106**, 085501 (2011).
[21] K. F. MacDonald, Z. L. Samson, M. I. Stockman, and N. I. Zheludev, Nat. Photonics **3**, 55 (2009).
[22] M. I. Stockman, M. F. Kling, U. Kleineberg, and F. Krausz, Nat. Photonics **1**, 539 (2007).
[23] T. Y. Hwang, A. Y. Vorobyev, and C. Guo, Appl. Phys. Lett. **95**, 123111 (2009).
[24] A. Y. Vorobyev and C. Guo, Appl. Phys. Lett. **92**, 041914 (2008).
[25] Z. L. Samson, P. Horak, K. F. MacDonald, and N. I. Zheludev, Opt. Lett. **36**, 250 (2011).
[26] S. N. Andreev, V. I. Belotelov, D. A. Bykov, L. L. Doskolovich, V. P. Tarakanov, and A. K. Zvezdin, J. Opt. Soc. Am. B **28**, 1111 (2011).
[27] T. Brixner, F. J. Garcia de Abajo, J. Schneider, and W. Pfeiffer, Phys. Rev. Lett. **95**, 093901 (2005).
[28] P. Bharadwaj, B. Deutsch, and L. Novotny, Adv. Opt. Photon. **1**, 438 (2009).
[29] L. Novotny and N. van Hulst, Nature Photon. **5**, 83 (2011).
[30] E. S. Unlu, R. U. Tok, and K. Sendur, Opt. Express **19**, 1000 (2011).
[31] K. Sendur, C. Peng, and W. Challener, Phys. Rev. Lett. **94**, 043901 (2005).
[32] K. Sendur, W. Challener, and C. Peng, J. Appl. Phys. **96**, 2743 (2004).
[33] E. D. Palik, *Handbook of Optical Constants of Solids* (Academic Press, New York, 1998).